AIAA JOURNAL
Vol. 40, No. 2, February 2002

Numerical Investigation of Turbulent Mixing in a Jet/Wake Vortex Interaction

C. Ferreira Gago,* S. Brunet,* and F. Garnier†
ONERA, 92320 Châtillon, France

A three-dimensional temporal numerical simulation of the interaction between a jet and a vortex wake is described to contribute to the understanding and modeling of engine jet dispersion of an aircraft in cruise condition. First, a comparison of the numerical results with a wind-tunnel experiment is presented. Experimental data comprise turbulent rates measured by a laser Doppler velocimeter and mean temperature fields delivered by thermocouples. The calculation is in quite good agreement with the experiment. Second, the passive scalar distribution (initially included in the jet) in the vortex wake is focused on. The turbulence induced by the jet flowfield interacts with the vortex, resulting in large-scale structures generated outside the vortex core, whereas the region very close to the core keeps its laminar state. The passive scalar concentrates in the large-scale structures where azimuthal and axial (positive and negative) vortices are combined. The resulting scalar field distribution shows no scalar inside the vortex core.

I. Introduction

THE increase of pollution in the atmosphere has received particular attention in recent years.[1,2] One aspect concerns the presence of aircraft emissions in a very sensitive region of the upper troposphere or the lower stratosphere. Throughout artificial cirrus cloud formation, perturbations produced by these effluents may have an effect on climate change if they are large enough to modify the Earth's radiative budget.[3] However, the formation of the new particles (aerosols or contrails) in the aircraft wake remains unclear and needs more study.[4] In past years, several studies have been performed to build a theoretical understanding of the mechanisms responsible for this particle formation. In addition to the formation process itself, attention has been given to other important phenomena such as the turbulent mixing of the engine exhaust in the trailing vortex.

The characterization of subsonic aircraft's impact on the atmosphere needs numerical tools, which must be able to predict, with acceptable confidence, the turbulent mixing mechanism. These are complex and involve several distinct processes. It is convenient to identify two overlapping regimes[5]: the jet and deflection regimes. The first one is that of usual coflowing jets, and it scales with the jet diameter. Later, the exhaust jet is entrained into the wake vortex and characterizes the second regime. The convection and shearing processes associated with the tangential velocity field of the trailing vortex strongly affect the jet flow behavior.

The computation of this complex flow has been undertaken by various authors.[2–6] Garnier et al.[5] and Miake-Lye et al.[6] solved the average governing equations to describe the mixing processes in the near field of aircraft wake. Other authors[7,8] used a different approach based on the large-eddy simulation method to examine the trailing vortex interaction with engine jet in the far field of aircraft wake. However, in spite of the progress made in the understanding of the turbulence mechanism in a wake vortex, an essential dearth of information still exists, especially dealing with the role of large-scale structures on a scalar field distribution. The latter helps in explaining the entrainment and mixing processes of the engine emissions in the vortex.

The work presented here attempts to give a physical insight into how the mixing of the engine jet is affected by the three-dimensional turbulence and the vortex flowfield.

The Reynolds number of flows of aeronautic and environment interest is often very high. However, many physical phenomena are also observed in flows at low Reynolds number, and to achieve this purpose, one may use the direct numerical simulation (DNS). The numerical simulation of the flow is performed using a three-dimensional temporal DNS of the compressible Navier–Stokes equations. The computation is advanced in two steps: the first step is stopped when it provides an estimation of the end of the jet regime; in the second step interaction with a Lamb–Oseen vortex field is accounted for.

An experiment detailed by Brunet et al.,[9] delivers a database that can be used for improving such computation tools. The wake of a generic model corresponding to a rectangular planform NACA 0012 equipped with two heated jets is investigated. The experimental results comprise mean and fluctuating velocity fields [measured with a laser Doppler velocimeter (LDV) system] and mean temperature field (measured with thermocouples). Unsteady aspects of the flow are also described by means of hot-wire measurements. Thereafter, numerical results are compared with the experimental database, and the passive scalar distribution in the flow is discussed. In a numerical simulation it is difficult to reproduce the test operating conditions exactly. Direct comparison with experimental data then becomes somewhat superficial. One important difference is the way the flow evolves. In a temporal simulation, the flow is computed in a reference frame moving at the mean flow speed and flow periodicity is assumed. In an experimental device, the flow evolves spatially downstream, and turbulence data are collected over different time sequences, at the same spatial location. A more accurate comparison would be achieved by performing a spatial simulation. Nevertheless, the expanse of the flow studied here would then require a number of mesh points, which makes such a calculation feasible not anymore. Furthermore, some authors (for example, see Michalke and Hermann[10] or Cortesi et al.[11]) have shown that the numerical simulation based on the time-dependent approach could be a useful tool for interpreting turbulence phenomena if some restrictions have been applied.

The structure of the paper is as follows. In Sec. II, the governing equations and the numerical solution technique are outlined. The accuracy issue concerning the numerical techniques involved for the transport equation is discussed briefly. In Sec. III, a comparison with experimental data is presented, and attention is turned to the role played by large-scale structures on the mixing process. Finally, in Sec. IV, the conclusions are presented.

Received 18 October 2000; revision received 8 June 2001; accepted for publication 8 June 2001.

*Ph.D. Student, Atmospheric Environment Unit, Physics Department, 29, avenue de la Division Leclerc.

†Senior Scientist, Atmospheric Environment Unit, Physics Department, 29, avenue de la Division Leclerc.

II. Model Review and Numerical Methods

The flow is governed by the fully compressible Navier–Stokes equations. The mass, momentum, and total energy equations are written in nondimensional form for a Cartesian coordinate system:

$$\frac{\partial \rho}{\partial t} + \frac{\partial \rho u_j}{\partial x_j} = 0 \tag{1}$$

$$\frac{\partial \rho u_j}{\partial t} + \frac{\partial}{\partial x_j}[\rho u_i u_j + p\delta_{ij}] = \frac{1}{Re}\frac{\partial \tau_{ji}}{\partial x_j} \tag{2}$$

$$\frac{\partial E}{\partial t} + \frac{\partial}{\partial x_j}[(E+p)u_j] = \frac{1}{Re}\frac{\partial u_i \tau_{ji}}{\partial x_j} + \frac{1}{(\gamma-1)PrReM^2}\frac{\partial^2 T}{\partial x_j^2} \tag{3}$$

where $E = [p/(\gamma-1)] + \frac{1}{2}\rho u_i u_i$ and τ_{ji} is the viscous stress tensor. With the law for perfect gas, the pressure reads

$$p = \rho T/\gamma M^2 \tag{4}$$

where $\gamma = C_p/C_v$ is the ratio of specific heats and T is the temperature. Re, Pr, and M are the Reynolds, Prandtl, and Mach numbers, respectively. Furthermore, our simulation is performed by using a low subsonic Mach number of 0.2, which should make the calculation close to the incompressible limit. Nevertheless, the weakness of temperature gradients considered in our study allows us to assume the viscosity to be constant.

Scalar Mixing

For simplicity and to introduce a general approach, the flowfield is considered here as a binary mixture. Thus a two-stream problem is examined that has uniform properties over one part of the flowfield, which is called the jet stream, and different uniform properties over the rest of the flowfield, called the external flow stream. Initially, one assumes that there are no exhaust products in the external airstream and no ambient air in the jet stream.

Based on analysis of mixing, the following assumptions are applied:

1) The mass diffusion velocities of species are expressed in terms of Fick's law.

2) Thermal diffusion of emissions is neglected.

3) The diffusion coefficients D_i of the different species with respect to the mixture are constant and equal. ($D_i = D$ for all of the species of the jet and the external flow.)

4) Specific heats at constant pressure for all species take the same value C_p.

5) In many calculations concerning gases, the Lewis number Le is taken to be equal to one. The Lewis number has a real measurable value for a given fluid (often close to one for gases) and is only taken to be an approximate value for particular purposes.

This approximation is frequently helpful in theoretical mixing and combustion analyses.[12] Lewis number can be defined from Prandtl number Pr and Schmidt number Sc: $Le = Sc/Pr$. In this analysis, we will take $Pr = 0.7$. It is convenient to introduce the mixture variable Z (or the dilution ratio)

$$Z = \frac{F_j + F_{a,0}}{F_{j,0} + F_{a,0}} \tag{5}$$

where F_j, $F_{j,0}$, and $F_{a,0}$ describe, respectively, the mass fraction of exhaust species, the initial mass fraction of exhaust species, and the mass fraction of ambient species. Z is defined as a passive scalar, which is initially assumed to have a value of zero in the external flow and reaches a maximum of one at the center of the jet. Furthermore, this conserved scalar does not influence the flow dynamics. This variable satisfies the following conservation equation:

$$\frac{\partial \rho Z}{\partial t} + \frac{\partial \rho Z u_j}{\partial x_j} = \frac{1}{ReSc}\frac{\partial}{\partial x_j}\left(\mu \frac{\partial Z}{\partial x_j}\right) \tag{6}$$

Numerical Technique and Boundary Conditions

In convective terms, spatial derivatives are taken with sixth-order compact finite differences.[13] To minimize the aliasing error, we follow the procedure applied by Boersma and Lele.[14] Thus, the nonlinear terms have been rewritten in skew symmetric form, that is,

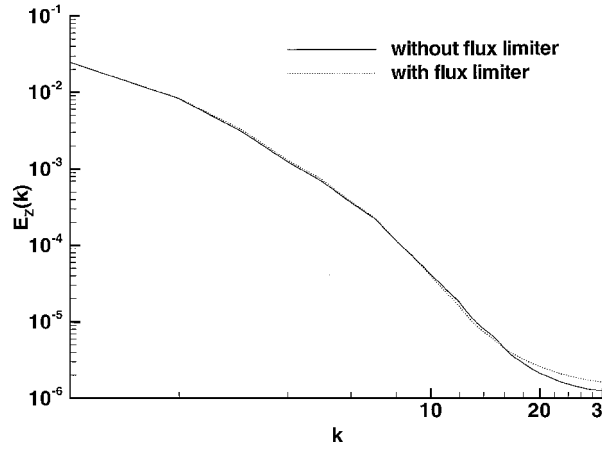

Fig. 1 One-dimensional normalized spectra of the scalar Z; spectra computed by using or not using a flux-limiter method for the convection–diffusion equation.

$$\frac{\partial \rho u_i u_j}{\partial x_j} = \frac{1}{2}\left(\frac{\partial \rho u_i u_j}{\partial x_j} + u_i \frac{\partial \rho u_j}{\partial x_j} + \rho u_j \frac{\partial u_i}{\partial x_j}\right) \tag{7}$$

Diffusive terms are discretized by using a second-order accurate finite difference scheme. This also helps to damp plausible instabilities. The time integration is carried out with a third-order Runge–Kutta method (see Ref. 15).

The main problem in resolving the transport equation, that is, Eq. (6), is the bounded discretization of convection terms in steep gradient zones. Such a critical situation is encountered in the exhaust jet mixing within a vortex flow.[16] In the present work, a superbee flux-limiter algorithm[17] of second order is retained. It prevents nonphysical oscillations and maintains positivity of the passive scalar. To gain confidence in the accuracy of the flux-limiter algorithm involved in solving Eq. (6) and to check if the more energetic scales in the flow are adequately resolved, one-dimensional spectra of the passive scalar have been performed. Typical scalar spectra are shown in Fig. 1, where a comparison between two simulations using or not using the flux-limiter algorithm has been plotted. The energy distribution at low wave numbers is practically identical. However, when using the flux-limiter scheme, a small energy accumulation is detected at the highest frequency.

In the axial, that is, streamwise, direction, periodicity is assumed, as usually done in temporal developing jets flows. The wavelength in the streamwise direction, that is, the length of our control volume, is based on Michalke and Hermann's[10] stability analysis for a spatially evolving jet. By using Gaster's[18] transformation, we obtain the wavelength of maximum growth of the first azimuthal disturbance. To observe a pairing event, the downstream size of the computational domain is taken equal to twice this wavelength.[19,20] Note that the pressure field is obviously not periodic. However, we can assume that variations around the pressure field gradients could be periodic. Finally, nonreflexive conditions introduced by Thompson[21] are used at the lateral boundaries of the computational domain.

Initial Conditions

Only one-half of the flow, that is the interaction of one jet with one vortex, has been computed. Forcing a single grid to conform to both the jet and the vortex flows would be extremely difficult. Thus, when the procedure used by Myake-Lye et al.,[6] Lewellen and Lewellen,[8] Garnier et al.,[5] and Gerz et al.[7] is used, the computation is performed in two steps. A schematic of the flow configuration is presented in Fig. 2.

In a first step one computes the jet development alone, without accounting for the vortex field, that is, the jet regime, as defined in Sec. I. For this jet regime simulation, the equations are nondimensionalized by scaling the velocities with the centerline velocity, and the length scale is equal to the radius R. The former is expressed as the middle of the jet shear layer defined by $U(R) = \frac{1}{2}(U_j + U_0)$, where U_j and U_0 are, respectively, the jet core velocity and the external flow velocity.

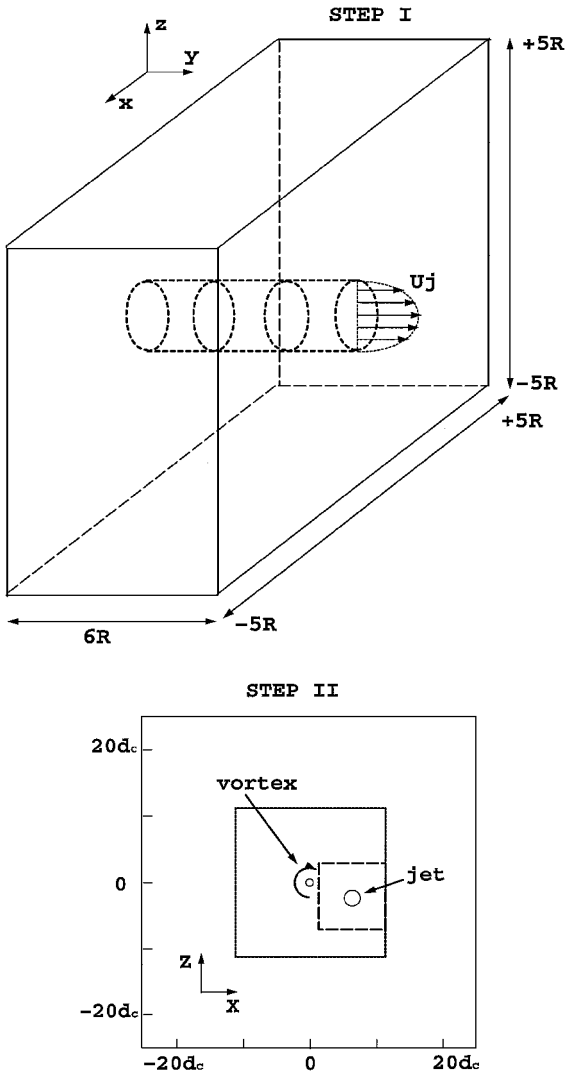

Fig. 2 Schematic of the flow configuration. Step I, simulation of the jet and step II, simulation of the interaction of the jet with the vortex flowfield; for step II, the initial position of the jet relative to the vortex center is provided by the experimental data.

In the following, we use the initial velocity profile

$$U(r) = \tfrac{1}{2}(U_j + U_0) - \tfrac{1}{2}(U_j - U_0)\tanh\left[\tfrac{1}{4}(R/\theta)(r/R - R/r)\right] \quad (8)$$

The distance r is related to the Cartesian coordinates by the relation $r = \sqrt{(x^2 + z^2)}$, and θ is the momentum boundary-layer thickness of the jet shear layer:

$$\theta = \int_0^\infty \left\{\frac{U - U_0}{U_j - U_0}\right\}\left\{1 - \frac{U - U_0}{U_j - U_0}\right\} \mathrm{d}r \quad (9)$$

Note that the static case $U_0 = 0$ has been investigated by several authors[22–24] and seems to model the circular jet flow in the potential core region quite well, as was shown by Moore.[25] We restrict the present investigation to one value of the jet parameter, namely, $R/\theta = 10$. Indeed, among the cases studied by Michalke and Hermann,[10] this value corresponds to the most unstable jet velocity profile. Random Gaussian shape perturbations are imposed on the three components of the velocity field. The initial distribution of the passive scalar follows a law identical to that of velocity. The computational domain is rectangular, and the grid is uniform in all directions. As explained in the preceding section, the streamwise extent of the computational box is $L_y = 6R$, with 61 nodes, corresponding to a mesh of $\Delta_y = 0.1R$. The cross plane extends from $x, z = -5.1R$ to $x, z = 5.1R$ and is defined with 137×137 nodes, corresponding to a space step of $\Delta_{x,z} = 0.075R$. The first step of the computation is performed using a Reynolds number based on the radius R and equal to $Re = U_j R/\nu = 10^3$.

The jet development, obtained with the first step, is then compared to the experimental results by considering the profiles $\tilde{U} = (U - U_0)/(U_j - U_0) = f(y/r_j)$, where U_0, U_j, and r_j are the freestream velocity (20 m/s), the jet exit velocity (60 m/s), and the jet nozzle radius (5×10^{-3}m), respectively. Coupling with the vortex starts when $\tilde{U} = 0.112$, which corresponds to $y/b = 0.5$, the first cross section measured downstream. This also corresponds to $y/r_j = 50$, a reasonable characteristic distance for the end of the jet regime. Then interaction with the vortex wake is taken into account, and a Lamb–Oseen vortex is fitted on the transverse part of the experimental velocity field. Here, the reference quantities are defined in the first station at $y/b = 0.5$. The diameter of the vortex core, $d_c = 12$ mm, is chosen as the length scale. The reference velocity $U_{\theta\max}$ corresponds to the maximum tangential velocity measured in the experiment. It is deduced from the relation

$$U_{\theta\,\max} = \Gamma_c/2\pi d_c \quad (10)$$

where $\Gamma_c = 0.68$ m^2 s^{-1} is the vortex circulation measured at the viscous radius r_c.

The computation grid is enlarged to 327×327 nodes, in the cross planes. It is uniform in the domain $-11.1d_c \le x, z \le 11.1d_c$, with a mesh of $0.075d_c$. Then it is stretched using a monotonic tanh law, up to $25.1d_c$. The core of the Lamb–Oseen vortex comprises approximately 21 node points (an equivalent value to that used by Ragab[26]). The circulation-based Reynolds number $Re = \Gamma_c/\nu$ of the computation is equal to 5×10^3.

The time step is $\Delta t = 0.005$, and the Courant–Friedrichs–Lewy number is 0.4. The simulation of this second step of the flow uses 2.8-GB memory and needs 25 s CPU time per time step, on a NEC SX-5 series computer.

III. Results and Discussion

In the present study, we have performed a temporal simulation of the flow, depending on the time variable t/t_0, where t_0 is the timescale given by $t_0 = d_c/U_{\theta\max}$. On the other hand, the spatial evolution of the flow, observed in the experiment, depends on the spatial variable y/b, where b denotes the span of the model wing ($b = 50$ cm). Because we want to compare the experimental results with the numerical ones, a relation between t/t_0 and y/b must be established, according to the Taylor assumption[27] (also see Ref. 28). If U_0 denotes the experimental freestream velocity ($U_0 = 20$ ms^{-1}), the time variable t/t_0 and the axial position y/b are related by

$$t/t_0 = \{[y/b - (y/b)_0] \times b/(U_0 \times t_0)\} \quad (11)$$

with $(y/b)_0 = 0.5$. When the jet vortex simulation starts, we have $t/t_0 = 0$, as already explained, it corresponds to $y/b = 0.5$. In what follows, we will refer mainly to the axial position y/b.

Comparison with Experimental Data

Figure 3 shows a comparison of the experimental and numerical axial velocity profiles as a function of the jet radius r (initial jet radius is r_j). The experimental one is obtained at the station $y/b = 0.5$. The numerical velocity profile is computed as follows. First, the instantaneous velocity is averaged in the axial direction y. Second, the averaged velocity is interpolated into a polar grid. Third, later velocity is averaged in the azimuthal θ direction, to obtain a profile, which is a function of r. No averaging in time is performed; therefore, the mean profile is a function of time (or spatial location). The experimental jet being slightly distorted by the vortex flow at $y/b = 0.5$ (shown subsequently), the velocity profiles shown in Fig. 3 mark the end of the jet regime calculation, characterized by the value $\tilde{U} = 0.112$. As already explained, the interaction with a Lamb–Oseen model is then taken into account.

The numerical and experimental tangential velocity profiles are shown in Fig. 4, at the two locations $y/b = 0.5$ and 8. The initial Lamb–Oseen velocity distribution is labeled "Numerical simulation: $y/b = 0.5$" in Fig. 4. A half-circle has been added showing the initial position of the jet. The distance between the jet and the vortex centers is equal to 14 vortex core radii r_c and corresponds effectively

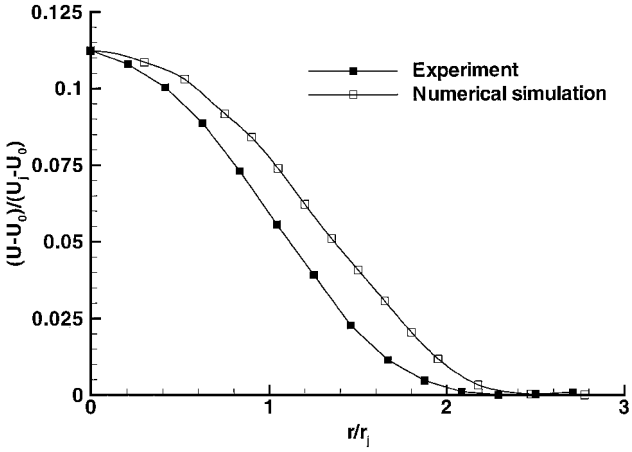

Fig. 3 End of the jet regime: mean velocity profiles at $y/b = 0.5$.

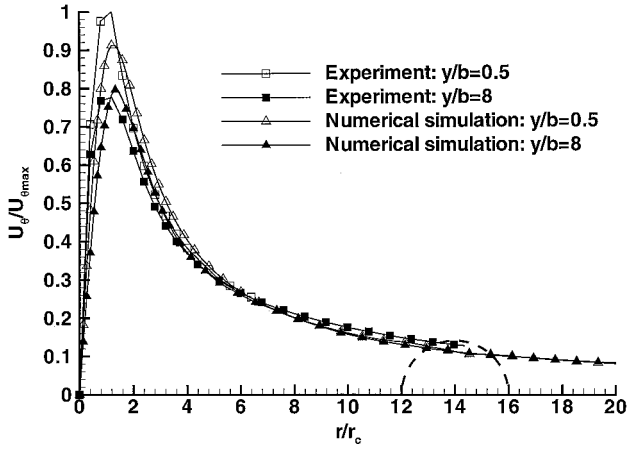

Fig. 4 Computational Lamb–Oseen vortex fit of the experimental velocity field at $y/b = 0.5$ and 8; jet located at $r/r_c \approx 14$; dashed circle shows the diameter and the initial position of the jet relative to the vortex center, provided by the experimental data.

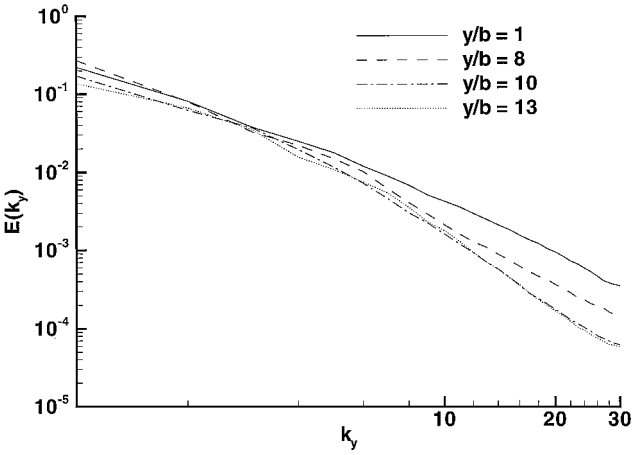

Fig. 5 One-dimensional spectra for the computational velocity field.

to that measured in the experiment, at 0.5 wingspan downstream. A quite good agreement between experimental and numerical profiles is observed in the potential region of the vortex. In the later region the tangential velocity follows a law in $1/r$. It takes place when the radius r is greater than the vortex core radius r_c.

Figure 5 presents one-dimensional energy spectra $E(k_y)$, computed at different times during simulation (referenced by spatial location in Fig. 5). The spectrum is obtained by taking the Fourier transform of the velocity field in the axial direction and integrating the Fourier coefficients in the x, z plane. The low energy content

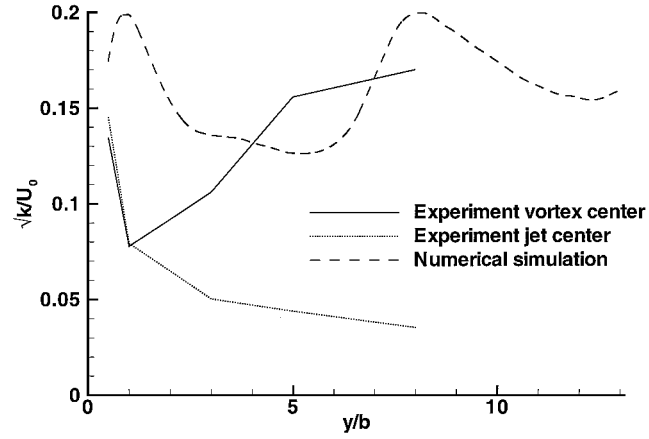

Fig. 6 Downstream evolution of total turbulent kinetic energy.

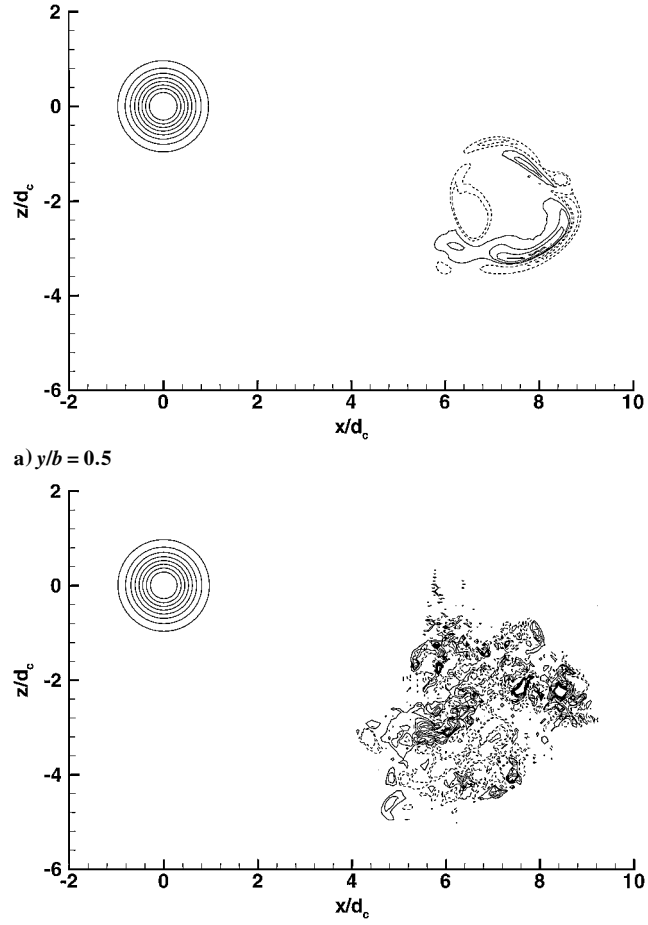

Fig. 7 Numerical axial component of vorticity Ω_y, in a meridional plane normal to the axial direction where dashed lines correspond to negative values of Ω_y and contours range from -1 to 4 in steps of 0.5.

at the higher-wave-number end of spectra indicates that the flow is well resolved.

Figure 6 shows the numerical downstream evolution of the turbulent kinetic energy. It is obtained by adding the values of the one-dimensional spectrum for all wave numbers. Thus, kinetic energy can be expressed only as a function of time (or spatial location). The turbulent rates measured by LDV in the jet centerline and in the vortex center are also shown.[9]

Examining the evolution of turbulent kinetic energy provided by the computations, one could display three stages. At first, and until $y/b \approx 1$, the integrated energy exhibits a brief increase mainly generated by the growth of the most unstable mode, which develops within the jet flowfield. Furthermore, we have plotted in Fig. 7

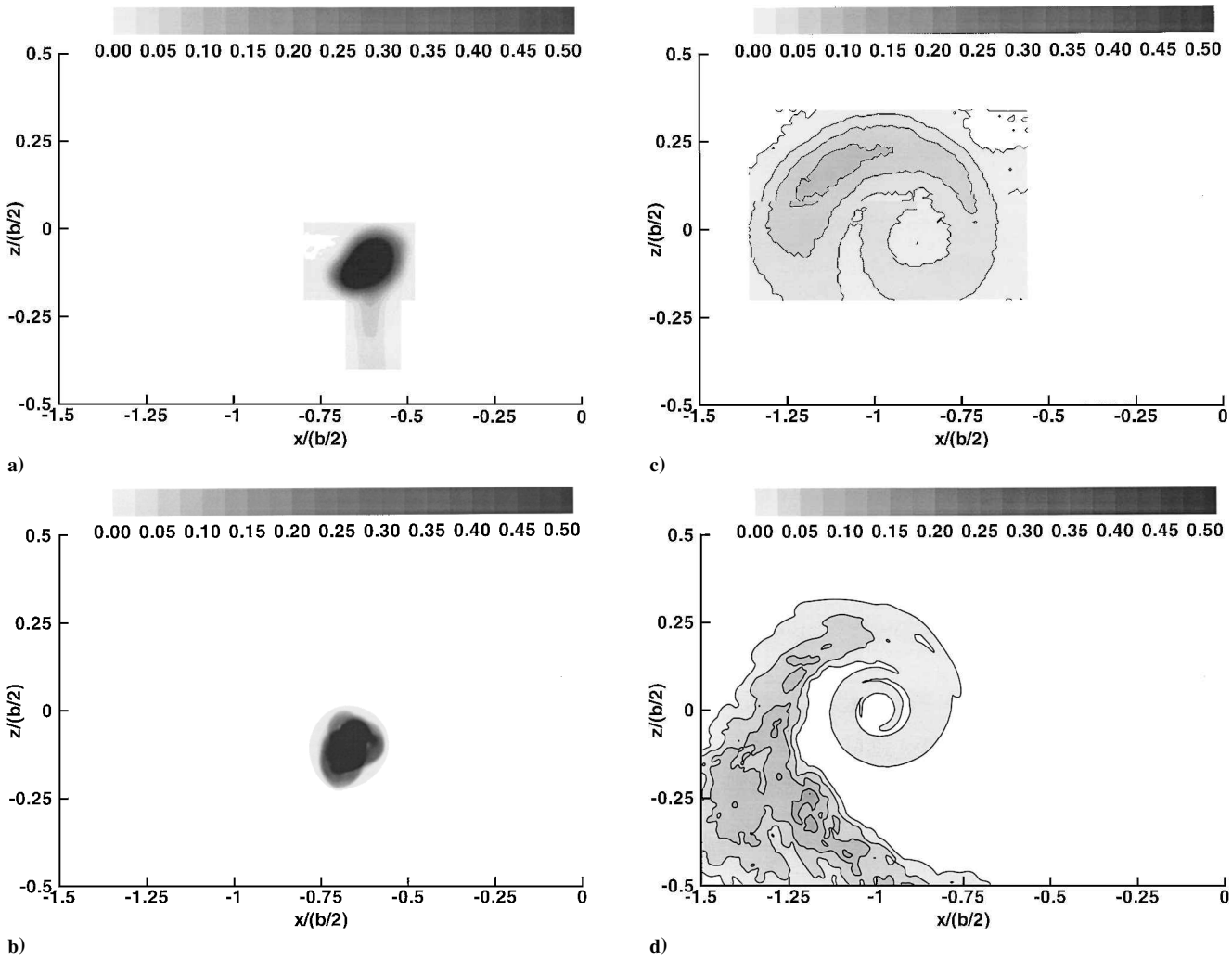

Fig. 8 Comparison between downstream cross sections of the experimental temperature tracer: a) $y/b = 0.5$ and c) $y/b = 8$; and downstream averaged of the computational passive scalar field: b) $y/b = 0.5$ and d) $y/b = 8$.

the numerical longitudinal component of vorticity Ω_y at stations $y/b = 0.5$ and 1, in a meridional plane normal to the axial direction. At the center of the computational domain, that is, $x/d_c = 0$ and $z/d_c = 0$, positive and concentric contours represent the vorticity distribution of the vortex core. The presence of the most unstable mode, that is, the most energetic, within the jet, is highlighted in Fig. 7a, where the longitudinal component of vorticity is relatively well organized in two fields: one positive and the other negative. During energy increase, that is, up to the station $y/b = 1$, the jet flow will keep its vorticity field nearly coherent with large-scale structures.

In Fig. 7b, the bursting of the structures is shown, characterizing the fully turbulent state of the jet. In the experiment, the jet is already fully turbulent at $y/b = 0.5$. Thus, no comparison with experimental data can be performed between $y/b = 0.5$ and 1. In Fig. 6, the kinetic energy undertakes then to decrease until three wingspans downstream. A similar trend is observed for the turbulent rate measured in the center of the jet. The energy fall is probably accelerated by the presence of the rotational component of the vortex field. This first stage, between $y/b = 0.5$ and 6 characterizes the tangential velocity influence of the vortex on the jet development. Until $y/b \approx 6$, the vortex core doesnot move. Indeed, the turbulent jet field does not affect the Lamb–Oseen model.

As the downstream distance increases, that is, between the stations $y/b \approx 6$ and 8, the vortex center starts to oscillate in the cross planes, with maximum amplitude of the order of $\Delta r \approx \frac{1}{3} d_c$ (data not shown). This oscillatory movement involves an increase of turbulent kinetic energy, also measured experimentally in the center of the vortex. This seems consistent with Devenport et al.[29] and Youssef et al.[30] experimental and computational results, which will be discussed more precisely in the next section. This second stage could be characterized by the influence of the turbulence generated by the jet flow upon the vortex behavior. Finally, in a third stage, beyond eight wingspans downstream, the turbulent kinetic energy saturates, and then a period of decay sets in.

The experimental cross sections of the dimensionless temperature at $y/b = 0.5$ and 8 are presented in Figs. 8a and 8c. At this stage, the temperature variations are sufficiently weak (less than 10%, see Brunet et al.[9]). Consequently, the temperature acts as a passive scalar and could be compared with the computed passive scalar Z of Eq. (6). Furthermore, such an assumption has already been made by Cortesi et al.[11] The corresponding numerical results are shown in Figs. 8b and 8d, where averages along the periodic direction y have been performed. The entrainment process shows a stretching and distortion of the interface between jet and external flow, followed by a relatively large-scale engulfment into the rotational region (Figs. 8c and 8d). Furthermore, the comparison between Figs. 8c and 8d shows that the qualitative features of the jet entrainment are relatively well predicted by the numerical simulation at eight wingspans. Nonetheless, the entrainment of the computed jet flow by tangential momentum is slightly delayed. Examining the experimental and numerical mean profiles of the jet axial velocity at 0.5 wingspan, as shown in Fig. 3, we can notice that the computational result seems to overpredict the experimental one. As a consequence, an excess of axial momentum is then produced within the jet leading the delay of the entrainment process.

Figure 9 presents the downstream variations of temperature T peak values and those of Z peak values (both called tracer concentrations in Fig. 9). Here thermocouple measurements are comprised inside a ± 0.5 K error bar.[9] Numerical results appear

to be in a good agreement with the experimental ones. The present simulation gives a good estimation of the mixture variable downstream evolution.

Turbulent Mixing

The contours of axial vorticity and computational passive scalar, at different streamwise distances, are shown in Fig. 10 in a meridional plane normal to the axial direction. The solid lines indicate positive contours of vorticity, and the passive scalar is represented by flood contours. For plotting purpose, the computational domain is truncated to a smaller one: $-4d_c \le x, z \le 4d_c$. Until $y/b \approx 6$, the vortex core consists of positive concentric axial vorticity contours (Fig. 10a). The vorticity field and the contours of the passive scalar distribution associated to the turbulent jet are localized at the limit of the plot, beyond 4 vortex core diameters, that is, not shown in Fig. 10a, indicating that the jet flow is not yet trapped around the vortex core. As already discussed, kinetic energy variations six wingspans downstream characterize the rotational component influence of the trailing vortex, that is, the strong axial component of vorticity, on the jet turbulence. Because no significant increase of the energy is detected between $y/b \approx 3$ and 6 (see Fig. 6), we can deduce that, during this last period, the vortex keeps its laminar state and, consequently, preserves its positive and concentric axial vorticity contours. The turbulence induced by the jet flowfield has not yet reached the vortex core. Later (Fig. 10b), the jet interacts with the vortex core. This interaction results in the generation of small-scale motions all around the core. Both positive and negative vorticity contours are seen embedded within each other, which is a sign of small-scale motions as observed initially by Ragab and Sreedhar.[31] The region very close to the core retains its positive axial vorticity contours, but they are not concentric anymore. However, coherent vortical structures develop outside the vortex core region. They make up a pair of crowns characterized, respectively, by positive and negative axial vorticity (Fig. 10b). Those two crowns correspond to high axial vorticity levels, compared to those observed around the vortex core, and are approximately of the same amplitude. One can see in Fig. 10b that the scalar follows the new organized structures.

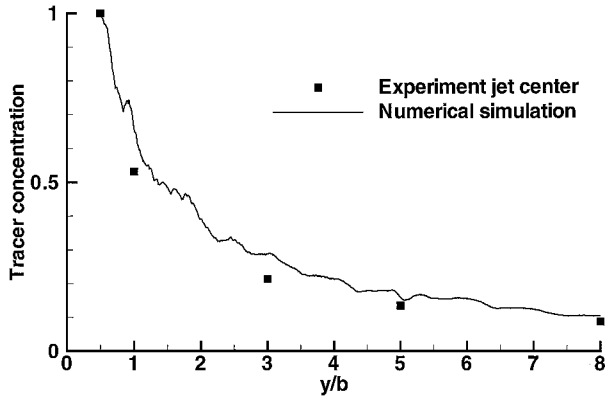

Fig. 9 Downstream evolution of the tracer concentration: comparison of the numerical vs experimental results.

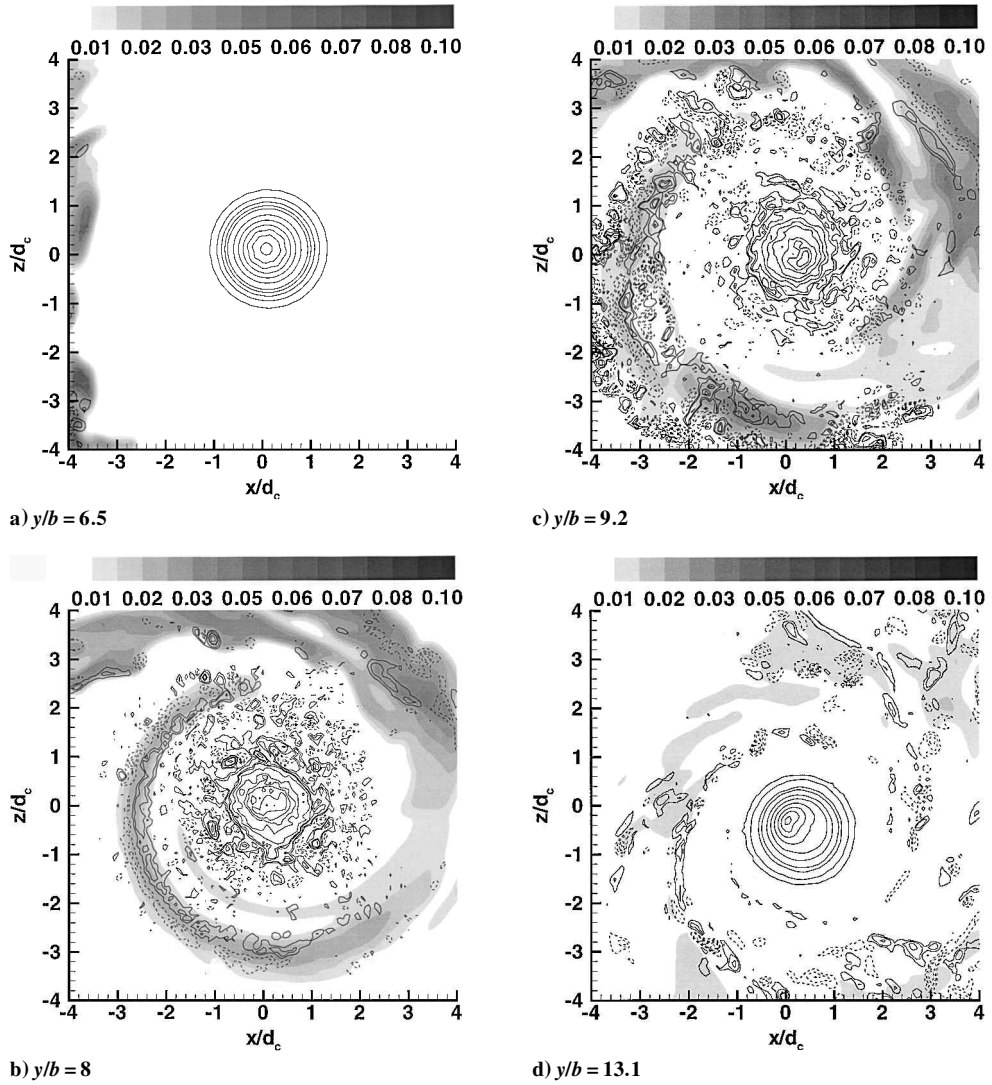

Fig. 10 Numerical axial component of vorticity Ω_y and computational passive scalar Z, in a meridional cross plane; dashed lines are negative values of Ω_y, and contours range from − 1 to 4 in steps of 0.2 for levels between − 1 and 1 and in steps of 0.5 for levels between 1 and 4. Passive scalar is represented by gray flood contours.

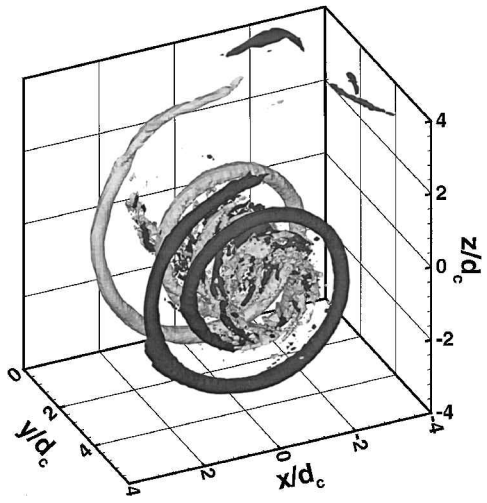

Fig. 11 Tridimensional view of the azimuthal vorticity component Ω_θ at $y/b = 7.7$; black and light gray surfaces correspond to azimuthal component Ω_θ equal to -1 and 1, respectively.

The crowns appear during the increase of the turbulent kinetic energy at approximately eight wingspans, as shown in Fig. 6. As already proposed in earlier work (for example, see Devenport et al.[29]), the high level of energy can result from buffeting of the vortex core generated by these crowns of large vortical structures. These later disappear as the simulation progresses downstream. In Fig. 10c, the region outside the core shows a mixture of positive and negative axial vorticity contours, and no more large-scale motions are generated. The breakup of these large-scale structures takes place when the decay energy period sets in, that is, at approximately $y/b \approx 13$. Finally, in Fig. 10d, the vortex core retrieves its initial contours of axial vorticity: The vortex returns to a laminar state. Indeed, the vortical structures lose coherence in a very short time, and stabilizing effect of the flow rotation suppresses the small-scale motions of turbulence. The relaminarizing tendency of the trailing vortex core has been observed experimentally[32,33] and numerically.[26–31] During all of the calculations, no scalar goes into the vortex core, and the latter always keeps its positive axial vorticity contours.

Next, contours of azimuthal component vorticity are discussed (Figs. 11 and 12). Until six wingspans, no azimuthal vorticity is observed in the vortex core (not shown here). Because of jet instabilities, vortical structures develop outside the core, as seen

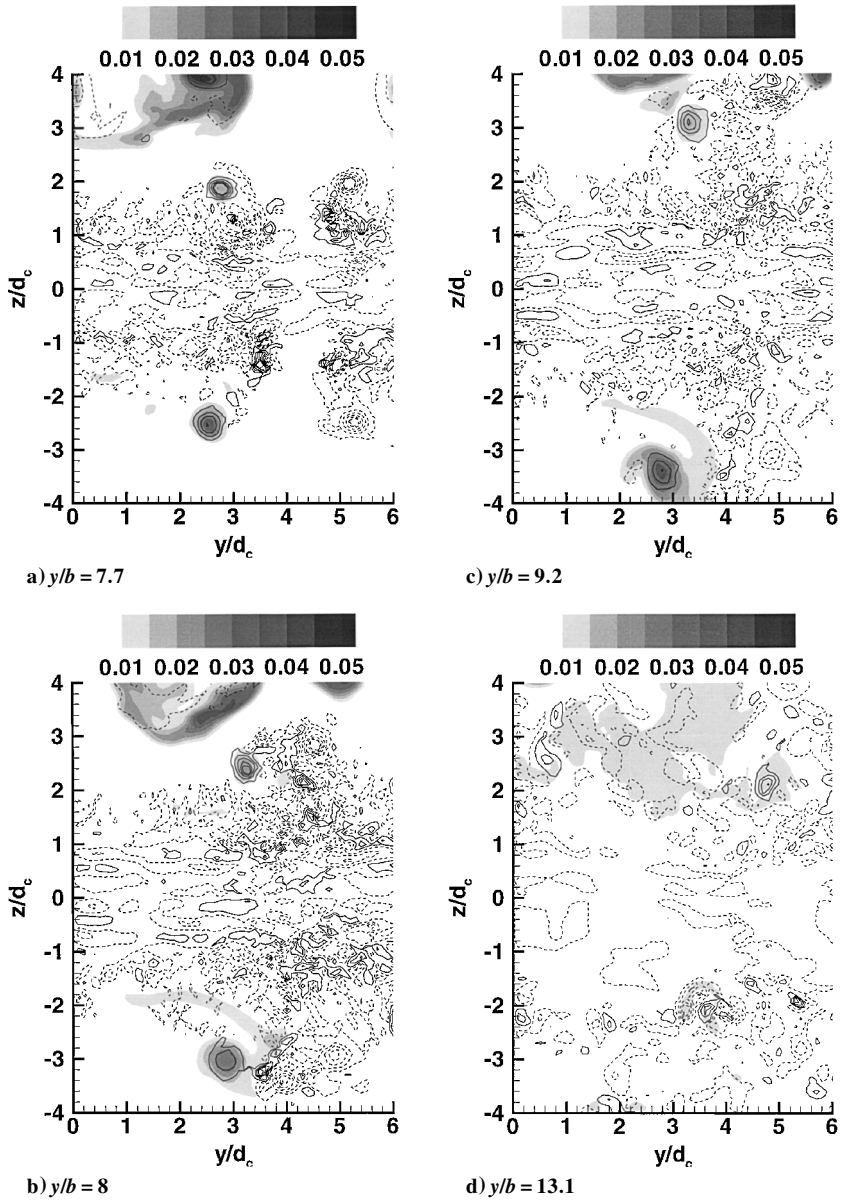

Fig. 12 Numerical azimuthal component of vorticity Ω_θ and computational passive scalar, in the plane $x/d_c = -1$; dashed lines are negative values of Ω_θ, and contours range from -3 to 3 in steps of 0.5. Passive scalar is represented by flood contours.

from azimuthal isovorticity surfaces at $y/b \approx 8$, in Fig. 11. Here, the light gray surface indicates a positive value and the black a negative one. Thus, these large-scale helical structures are counter-rotating vortices. The amplitude of those two isosurfaces is of the same order. Similar structures were detected by various authors.[30,34–36] As an example, in their study, Sreedhar and Ragab[34] observed the effect of random disturbances superimposed on the mean profiles of a Taylor vortex and of a Lamb–Oseen vortex. For the Taylor vortex, they[34] obtained structures similar to those presented in Fig. 11, but for the Lamb–Oseen vortex, the authors[34] detected no sign of the formation of new large-scale structures. Indeed, the simulation performed by Ragab[26] shows no significant turbulence growth for the Lamb–Oseen vortex. It is stable to linear and axisymmetric inviscid disturbances, but the addition of an axial component of velocity can make the Lamb–Oseen unstable and susceptible to linear disturbances (see Refs. 31–34). Nonetheless, in our numerical simulation, the generation of large vortical structures is due to the presence of an axial velocity profile superimposed initially in the vicinity of a two-dimensional Lamb–Oseen model.

In Fig. 12, the azimuthal component of vorticity is shown in a longitudinal plane, plotted at a cut $x/d_c = -1$. Contours of passive scalar are also presented. The organized helical structures positive and negative, which were so clearly visible in Fig. 11, are now seen in the streamwise cross-sectional cut. As the streamwise distance increases, mushroom structures can be identified outside the vortex core. They are formed by two counter-rotating azimuthal vortices at the top and the bottom of the plots. Simultaneously, both positive and negative of small-scale azimuthal structures are created inside the vortex core. Furthermore, one can also observe that the passive scalar concentrates only in the azimuthal vorticity of high positive levels, outside the vortex core. Ragab[26] has already remarked in his calculation that contours of high azimuthal vorticity correspond to regions of condensation of passive scalar. However, no scalar is seen inside the core. Later (Fig. 12d), those large-scale structures disappeared, and no more azimuthal vorticity is generated in the vortex core. The breakup process of these large-scale structures coincides with this of axial vorticity structures. It takes place during the decay of the turbulent kinetic energy at approximately 13 wingspans downstream.

Turning now to a zoom view of one large-scale structure developing outside the vortex core (Fig. 13), it can be noticed how the axial component (positive and negative) of the vorticity is enclosed in the azimuthal component one. The latter is chosen positive because the passive scalar seems to be trapped inside this azimuthal vortex. Here magnitude azimuthal (positive) vorticity is three times higher than the axial (negative and positive) one.

Finally, the resulting scalar field distribution shows no scalar inside the vortex core, as observed earlier in Figs. 10 and 12.

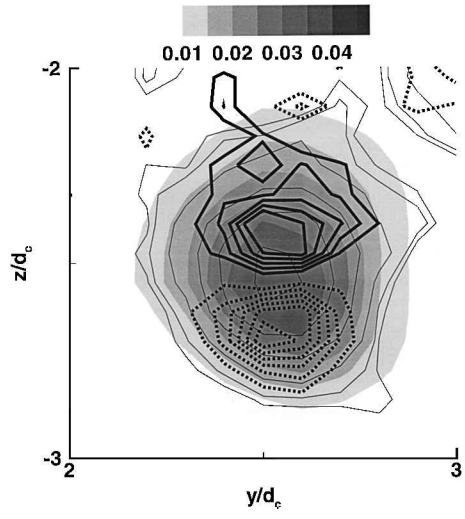

Fig. 13 Zoom view of a large-scale structure seen in Fig. 12a, where azimuthal vorticity (thin line, contours range from − 3 to 3 in steps of 0.5) and axial vorticity (thick line, contours range from − 0.6 to 0.6 in steps of 0.1) are superimposed to passive scalar contours.

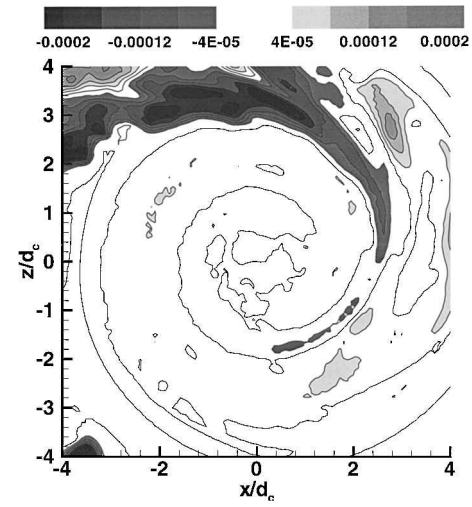

a) Radial component $\langle Z' u'_r \rangle$

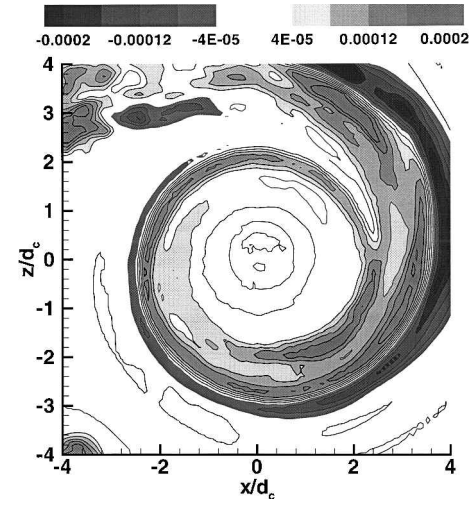

b) Axial component $\langle Z' u'_y \rangle$

Fig. 14 Scalar fluxes at $y/b = 7.7$.

In addition to the investigation of the scalar field distribution, we now look at the statistics of scalar concentration or the scalar fluxes. In this temporal simulation, these quantities are determined as follows. First we compute the Fourier transform of each velocity component u_i and scalar Z. We next obtain the scalar fluxes, which are defined as

$$|Z'u'_i| = \hat{Z}(x, z, k_y, t)\hat{u}^t_i(x, z, k_y, t) \tag{12}$$

where $\hat{Z}$, $\hat{u}^t_i$ and k_y are the Fourier transform of the scalar Z, the complex conjugate of the velocity Fourier transform, and the wave number in the axial direction, respectively. Finally $\langle Z'u'_i \rangle$ is computed by taking a simple average over all points in the axial direction. To characterize the turbulent fluxes in the vicinity of the vortex core, we focus on the axial $\langle Z'u'_y \rangle$ and radial $\langle Z'u'_r \rangle$ components of the scalar fluxes. Note that, the third component $\langle Z'u'_\theta \rangle$ has a negligible contribution compared to the two others (data not shown). Therefore we have only plotted (Figs. 14a and 14b) the radial and axial components of the scalar fluxes at $y/b \approx 8$, corresponding to the helical structure development (see Fig. 11). Near the vortex center, the value of the axial contribution is positive and more important than that of the radial contribution, which is closed to zero (Fig. 14a). Hence, the axial velocity produced by the turbulent jet through the vortex center probably dominates the transport mechanism of the scalar field.

IV. Conclusions

A numerical simulation of the interaction between a jet and a wake vortex has been performed.

Results have been compared to experimental data on heated jets interacting with the vortex wake of a generic wing. In the computation, the jet flow is marked by means of a passive scalar. The downstream evolution of this passive tracer is in quite good agreement with experimental results (temperature), even though the simulation shows a slightly delay in the entrainment of the computed jet flow by tangential momentum.

The Lamb–Oseen vortex is used as a model for a trailing vortex. The Lamb–Oseen is stable to linear and axisymmetric inviscid disturbances, but the addition of an axial component of velocity can make the vortex unstable and susceptible to linear disturbances. In our calculation, a jet profile is imposed in the vicinity of the Lamb–Oseen vortex. This results in the generation of large-scale structures all around the vortex core. These appear as counter-rotating vortex rings, where both azimuthal and axial vorticity occur. Note that the level of azimuthal vorticity is approximately three times higher than the axial one. The vortical structures are generated during the kinetic energy increase and seem to be responsible for the oscillatory movement of the vortex core. Such an enhancement is also measured in the experiment of Brunet et al.[9] As the downstream distance increases, the large-scale vortical structures disappear, and kinetic energy decays. This fall is in close correlation with an apparent return of the flow to a laminar state. The vortical structures rapidly lose coherence and the stabilizing effect of the flow rotation suppresses the small-scale motions of turbulence. During all of the simulation the vortex core keeps its positive axial vorticity.

Because the turbulent mixing processes involved in the interaction of a trailing vortex with an engine jet are of interest, we have considered a mixture variable (or passive scalar) Z, of which values are comprised between zero and one. To prevent nonphysical oscillations and maintain positivity of the passive scalar, a superbee flux limiter is used. Scalar spectra show that the more energetic scales in the flow are adequately resolved. Moreover, two dominating mechanisms have been highlighted: first the mixture variable concentrates in the vortical structures mentioned earlier, and no scalar is seen inside the vortex core. Furthermore, the axial velocity through the vortex core is seen to play an important role in the transport mechanism on the scalar field.

References

[1]Baumgardner, D., Myake-Lye, R. C., Anderson, M. R., and Brown, R. C., "An Evaluation of the Temperature, Water Vapor, and Vertical Velocity of Aircraft Contrails," *Journal of Geophysical Research*, Vol. 103, No. D8, 1998, pp. 8727–8736.

[2]Garnier, F., Beaudoin, C., Woods, P., and Louisnard, N., "Engine Emission Alteration in the Near Field of an Aircraft," *Atmospheric Environment*, Vol. 31, No.12, 1997, pp. 1767–1781.

[3]Seinfeld, J. H., "Clouds, Contrails and Climate," *Nature*, Vol. 391, Feb. 1998, pp. 837, 838.

[4]*Impact de la Flotte Aérienne sur l'Environnement Atmosphérique et le Climat*, French Academy of Sciences, No. 40, Paris 1997.

[5]Garnier, F., Brunet, S., and Jacquin, L., "Modelling Exhaust Plume Mixing in the Near Field of an Aircraft," *Annales Geophysicae*, Vol. 15, 1997, pp. 1468–1477.

[6]Miake-Lye, R. C., Martinez-Sanchez, M., Brown, R. C., and Kolb, C. E., "Plume and Wake Dynamics, Mixing, and Chemistry Behind a High Speed Civil Transport," *Journal of Aircraft*, Vol. 30, No. 4, 1993, pp. 467–479.

[7]Gerz, T., Dürbeck, T., and Konopka, P., "Transport and Effective Diffusion of Aircraft Emissions," *Journal of Geophysical Research*, Vol. 103, No. D20, 1998, pp. 25,905–25,913.

[8]Lewellen, D. C., and Lewellen, W. S., "Large-Eddy Simulations of the Vortex-Pair Breakup in Aircraft Wakes," *AIAA Journal*, Vol. 34, No. 11, 1996, pp. 2337–2345.

[9]Brunet, S., Jacquin, L., and Geffroy, P., "Experiment on Heated Jets/Wake Vortex Interaction," ONERA, Rept. RT 15/2496 DAFE/Y, 1999.

[10]Michalke, A., and Hermann, G., "On the Inviscid Instability of a Circular Jet with External Flow," *Journal of Fluid Mechanics*, Vol. 114, 1982, pp. 343–359.

[11]Cortesi, A. B., Smith, B. L., Yadigaroglu, G., and Banerjee, S., "Numerical Investigation of the Entrainment and Mixing Processes in Neutral and Stably-Stratified Mixing Layers," *Physics of Fluids*, Vol. 7, No. 3, 1999, pp. 162–184.

[12]Williams, F. A., *Combustion Theory*, 2nd ed., Addison-Wesley, Redwood City, CA, 1985, pp. 73, 74.

[13]Lele, S. K., "Compact Finite Difference Scheme with Spectral-Like Resolution," *Journal of Computational Physics*, Vol. 103, 1992, pp. 16–42.

[14]Boersma, B. J., and Lele, S. K., "Large Eddy Simulation of a Mach 0.9 Turbulent Jet," AIAA Paper 99-1874, 1999.

[15]Lowery, P. S., and Reynolds, W. C., "Numerical Simulation of a Spatially Developing Forced Plane Mixing Layer," Stanford Univ., Rept. TF-26, Stanford, CA, 1986.

[16]Brunet, S., Garnier, F., and Loraud, J. C., "Three Dimensional Direct Numerical Simulation of Plume Entrainment and Mixing in Trailing Vortices," *Computational Fluid Dynamics Journal*, Vol. 8, No. 3, 1999, pp. 410–418.

[17]Sweby, P. K., "High Resolution Schemes Using Flux Limiters for Hyperbolic Conservation Laws," *SIAM Journal on Numerical Analysis*, Vol. 21, No. 5, 1984, pp. 995–1011.

[18]Gaster, M., "A Note on the Relation Betweeen Temporally-Increasing and Spatially-Increasing Disturbances in Hydrodynamic Stability," *Journal of Fluid Mechanics*, Vol. 14, 1962, pp. 222–224.

[19]Verzicco, R., and Orlandi, P., "Direct Simulations of the Transitional Regime of a Circular Jet," *Physics of Fluids*, Vol. 6, No. 2, 1994, pp. 751–759.

[20]Martin, J. E., and Meiburg, E., "Numerical Investigation of Three-Dimensionally Evolving Jets Subject to Axisymetric and Azimuthal Perturbations," *Journal of Fluid Mechanics*, Vol. 230, 1991, pp. 271–318.

[21]Thompson, K. W., "Time Dependent Boundary Conditions for Hyperbolic System II," *Journal of Computational Physics*, Vol. 89, No. 2, 1990, pp. 439–461.

[22]Crighton, D. G., and Gaster, M., "Stability of Slowly Diverging Jet Flow," *Journal of Fluid Mechanics*, Vol. 77, 1976, pp. 397–413.

[23]Morris, P. J., "The Spatial Viscous Instability of Axisymetric Jets," *Journal of Fluid Mechanics*, Vol. 77, 1976, pp. 511–529.

[24]Plaschko, P., "Helical Instabilities of Slowly Divergent Jets," *Journal of Fluid Mechanics*, Vol. 92, 1979, pp. 209–215.

[25]Moore, C. J., "The Role of Shear-Layer Instability Waves in Jet Exhaust Noise," *Journal of Fluid Mechanics*, Vol. 80, 1977, pp. 321–367.

[26]Ragab, S., "Direct Numerical Simulation of Instability Waves in a Trailing Vortex," AIAA Paper 95-0591, 1995.

[27]Taylor, G. I., "Statistical Theory of Turbulence," *Proceedings of the Royal Society of London, Series A: Mathematical and Physical Sciences*, Vol. 164, No. A919, 1938, p. 476.

[28]Leboeuf, R. L., and Mehta, R. D., "On Using Taylor's Hypothesis for Three-Dimensional Mixing Layers," *Physics of Fluids*, Vol. 7, No. 6, 1995, pp. 1516–1518.

[29]Devenport, W. J., Zsoldos, J. S., and Vogel, C. M., "The Structure and Development of Counter Rotating Wing-Tip Vortex Pair," *Journal of Fluid Mechanics*, Vol. 332, 1997, pp. 71–104.

[30]Youssef, K. S., Ragab, S. A., Devenport, W. J., and Abdel Gawad, A. F., "Large Eddy Simulation of the Near Wake of a Rectangular Wing," AIAA Paper 98-0317, 1998.

[31]Ragab, S. A., and Sreedhar, M., "Numerical Simulation of Vortices with Axial Velocity Deficits," *Physics of Fluids*, Vol. 7, No. 3, 1995, pp. 549–558.

[32]Bandyopadhyay, P., Stead, D., and Ash, R., "The Organized Nature of Turbulent Trailing Vortex," AIAA Paper 90-1625, 1990.

[33]Devenport, W. J., Rife, M. C., Liapis, S. I., and Miranda, J., "Turbulent Trailing Vortices," AIAA Paper 94-0404, 1994.

[34]Sreedhar, M., and Ragab, S., "Large Eddy Simulation of Longitudinal Stationary Vortices," *Physics of Fluids*, Vol. 6, No. 7, 1994, pp. 2501–2514.

[35]Melander, V. M., and Hussain, F., "Polarized Vorticity Dynamics on a Vortex Column," *Physics of Fluids*, Vol. 5, No. 8, 1993, pp. 1992–2003.

[36]Dommermuth, D. G., and Yue, D. K., "A Numerical Study of Three Dimensional Viscous Interactions of Vortices with a Free Surface," *Proceedings of the 18th Symposium on Naval of Hydrodynamics*, National Academy Press, Ann Arbor, MI, 1990, pp. 727–788.

P. Givi
Associate Editor